Wave propagation reversal for wavy vortices in wide-gap counter-rotating cylindrical Couette flow

S. Altmeyer*
Institute of Science and Technology Austria (IST Austria), 3400 Klosterneuburg, Austria

Richard M. Lueptow†
Department of Mechanical Engineering and Department of Chemical and Biological Engineering, Northwestern University, Evanston, Illinois 60208, USA

(Received 28 October 2016; published 10 May 2017)

We present a numerical study of wavy supercritical cylindrical Couette flow between counter-rotating cylinders in which the wavy pattern propagates either *prograde* with the inner cylinder or *retrograde* opposite the rotation of the inner cylinder. The *wave propagation reversals* from prograde to retrograde and vice versa occur at distinct values of the inner cylinder Reynolds number when the associated frequency of the wavy instability vanishes. The reversal occurs for both twofold and threefold symmetric wavy vortices. Moreover, the wave propagation reversal only occurs for sufficiently strong counter-rotation. The flow pattern reversal appears to be intrinsic in the system as either periodic boundary conditions or fixed end wall boundary conditions for different system sizes always result in the wave propagation reversal. We present a detailed bifurcation sequence and parameter space diagram with respect to retrograde behavior of wavy flows. The retrograde propagation of the instability occurs when the inner Reynolds number is about two times the outer Reynolds number. The mechanism for the retrograde propagation is associated with the inviscidly unstable region near the inner cylinder and the direction of the global average azimuthal velocity. Flow dynamics, spatio-temporal behavior, global mean angular velocity, and torque of the flow with the wavy pattern are explored.

DOI: 10.1103/PhysRevE.95.053103

I. INTRODUCTION

Waves or wavy vortices appear as flow states in wide range of flow systems including shear flows, atmospheric flows, and rotating convection [1–4]. Usually these wavy states result from a hydrodynamic instability of rotationally invariant basic flow, i.e., the flow undergoes a supercritical Hopf bifurcation breaking the SO(2) symmetry [5–7]. It is well known that for the case of the inner cylinder rotating with the outer cylinder fixed the primary instability consisting of toroidal Taylor vortices acquires a waviness as the rotational speed of the inner cylinder increases with the waves propagating azimuthally in the same direction as the inner cylinder rotation. For a wide gap scenario the number of azimuthal waves is typically 2 to 7 [8], depending on the conditions by which the secondary transition is approached, and their azimuthal phase speed at mid-gap is about 0.25 to 0.5 times the surface speed of the inner cylinder [8–16]. (In the narrow gap case, particularly in the limit $\eta \to 1$, significantly larger azimuthal wave numbers can appear [17].)

A recent study [18] for a rotating inner cylinder and fixed outer cylinder clarified the transition from toroidal vortices in Taylor vortex flow (TVF) to toroidal wavy vortices in wavy vortex flow (WVF) for the mid- to narrow gap case (here radius ratios larger than 0.7). The waviness comes about due to the axial shear in the azimuthal velocity resulting from the alternate radial advection of azimuthal momentum by the Taylor vortices of the underlying Taylor-Couette flow. The wavy vortex pattern propagates in the direction of the rotation of the inner cylinder—the waves are *prograde* [8–16,19]. There are a few exceptions for which waves display *retrograde* propagation. For classical Taylor-Couette flow of a Newtonian fluid [18], counter-propagating waves have been predicted for wide gaps, and the transition to this situation always coincides with a *change* in the dominant azimuthal wave number as the radius ratio decreases. In another example, a recent study [20] detected wave propagation reversal in a complex fluid, a ferrofluidic flow triggered through an external magnetic field in which the same azimuthal wave number is maintained. A related example is that of Taylor-Couette flow with axial and radial imposed mass flux in which the azimuthal wave number reverses sign for large radial outflows and large axial flows so that the helicity of the vortices (not the wave propagation) changes from opposite that of the base flow to the same as the base flow [21].

Motivated by these cases, particularly the finding that in ferrofluidic Taylor-Couette flow the wave propagation reversal occurs while maintaining the same azimuthal wave number [20] for periodic boundary conditions, we consider wide-gap counter-rotating cylinders with a finite length annulus having fixed end walls. Although previous results indicate prograde wave propagation in a narrow-gap system [19], we show that continuously varying a single parameter, either the Reynolds number of the inner cylinder or the Reynolds number of the outer cylinder, in a wide-gap system reduces the azimuthal wave speed ω of the wavy instability until it reaches zero and eventually becomes negative. The overall angular velocity Ω of the flow shows qualitatively the same behavior, but the zero-crossing does not coincide exactly with that of the wavy instability. With further variation (in the same direction) in the parameter, the waves start to move in the *opposite* direction. In the case of constant outer cylinder rotation and large enough counter-rotation, the wavy flow goes from prograde to retrograde to prograde again as the speed of

*sebastian.altmeyer@ist.ac.at
†r-lueptow@northwestern.edu

the inner cylinder increases. The key points in the present study of wave propagation reversal are (i) the constant azimuthal wave number and (ii) the absence of any other additional applied forces (e.g., through-flow or magnetic forces) that can trigger the reversal.

The paper is organized as follows. Section II describes the basic equations and numerical method used in the present study. Section III presents numerical results starting with an introduction to the WVF states that were considered. Investigating the bifurcation scenario via $\mathrm{Re_i}$, we study the variation in flow dynamics and spatial-temporal characteristics that coincides with the wave propagation reversal. Finally, Sec. IV provides a discussion and conclusions.

II. GOVERNING EQUATIONS

Consider the flow driven in the annular gap between two independently rotating cylinders [22,23] of length L. The inner cylinder of radius R_i rotates at angular speed Ω_i and the outer cylinder of radius R_o rotates at angular speed Ω_o. The end walls enclosing the annulus are stationary. The fluid in the annulus is assumed to be Newtonian, isothermal, and incompressible with kinematic viscosity ν. Using the gap $d = R_o - R_i$ as the length scale and the radial diffusion time d^2/ν as the time scale, the non-dimensional Navier-Stokes equations governing the flow are

$$\partial_t \mathbf{u} + (\mathbf{u}\cdot\nabla)\mathbf{u} = -\nabla p + \nabla^2\mathbf{u}, \qquad \nabla\cdot\mathbf{u} = 0, \tag{2.1}$$

where $\mathbf{u} = (u,v,w)$ is the velocity in cylindrical coordinates (r,θ,z) and the corresponding vorticity is $\nabla\times\mathbf{u} = (\xi,\eta,\zeta)$. The system is governed by four independent non-dimensional parameters:

$$\begin{aligned} &\text{Inner Reynolds number:} && \mathrm{Re_i} = \Omega_i R_i d/\nu,\\ &\text{Outer Reynolds number:} && \mathrm{Re_o} = \Omega_o R_o d/\nu,\\ &\text{Radius ratio:} && R_i/R_o,\\ &\text{Aspect ratio:} && \Gamma = L/d. \end{aligned} \tag{2.2}$$

In the present study we fix the radius ratio to 0.5 (wide gap) and the aspect ratio to $\Gamma = 10$ while varying only the inner and outer Reynolds numbers.

Further, we consider non-rotating fixed endplates resulting in no-slip-fixed boundary conditions (FBC) with zero velocity at $z = \pm\Gamma/2$, which breaks the $O(2)$ axial symmetry of the (infinite) periodic Taylor-Couette system. The boundary conditions are $\mathbf{u}(r_i,\theta,z,t) = (0,\mathrm{Re_i},0)$, $\mathbf{u}(r_o,\theta,z,t) = (0,\mathrm{Re_o},0)$, and $\mathbf{u}(r,\theta,\pm\Gamma/2,t) = (0,0,0)$, where the non-dimensional inner and outer radii are $r_i = R_i/d$ and $r_o = R_o/d$, with $r_o - r_i = 1$.

The governing equations and the boundary conditions are invariant under arbitrary rotations R_α about the axis, reflections K_z about the annulus mid-plane $z = 0$, and with respect to time translations ϕ_{t_0}, generating the symmetry group $\mathrm{SO}(2)\times Z_2\times\mathbb{R}$, where the first two factors consist of the purely spatial symmetries, while the third factor corresponds to the temporal symmetries generating the one-dimensional translation group $\mathbb{R}$. The actions of the three symmetries on the velocity field are

$$R_\alpha(u,v,w)(r,\theta,z,t) = (u,v,w)(r,\theta+\alpha,z,t), \tag{2.3a}$$

$$K_z(u,v,w)(r,\theta,z,t) = (u,v,-w)(r,\theta,-z,t), \tag{2.3b}$$

$$\phi_{t_0}(u,v,w)(r,\theta,z,t) = (u,v,w)(r,\theta,z,t+t_0). \tag{2.3c}$$

A. Numerical method and classification

The Navier-Stokes equations (2.1) are solved using a second-order time-splitting method with consistent boundary conditions for the pressure [24,25]. Our code G1D3 [26] is a combination of a finite differences method in the radial and axial directions and a Fourier-Galerkin expansion in the azimuthal direction with a decomposition

$$f(r,\theta,z,t) = \sum_m f_m(r,z,t)\, e^{im\theta} \tag{2.4}$$

of all fields $f\in\{u,v,w,p\}$.

In order to characterize the different flow structures we consider two different quantities. First, as a global measure of the flow, we use the total modal kinetic energy

$$E_{\mathrm{kin}} = \sum E_m = \frac{1}{2}\sum_m \int_0^{2\pi}\int_{-\Gamma/2}^{\Gamma/2}\int_{r_i}^{r_o} \mathbf{u}_m\mathbf{u}^*{}_m r\,\mathrm{d}r\,\mathrm{d}z\,\mathrm{d}\theta, \tag{2.5}$$

where $\mathbf{u}_m$ is the mth Fourier mode of the velocity field. For the axisymmetric cases circular Couette flow (CCF) and TVF, only E_0 is nonzero.

Second, as a measure more closely related to the vortices and corresponding azimuthal and axial wave numbers, we use the azimuthal decomposition [Eq. (2.4)] of the radial velocity field. We perform an axial Fourier analysis of the mode amplitudes $u_m(z,t)$ at mid-gap, $r = r_1 + d/2$. We then identify for $m = 2$ and $m = 3$ the largest contribution in the axial Fourier spectrum of $u_m(z,t)$ for the patterns with $k = 3.148$ and $k = 3.769$. The oscillation of the corresponding complex Fourier amplitudes describe the frequencies $\omega_{m,k}$. It is this quantity that describes the wavy instability, and a change in its sign reflects the wave propagation reversal.

We identify the specific flow structures by the abbreviation (m,k). These modes reflect the symmetry properties of the vortex structures. Thus, e.g., the Fourier spectrum of the TVF solution contains a dominant $(0,k)$ mode and its complex conjugate $(0,-k)$. The spectrum of wavy vortex flow with two waves corresponding to azimuthal wave number $m = 2$ (designated $\mathrm{WVF_2}$) is dominated by $(2,k)$ and its complex conjugate $(-2,-k)$ as well as the underlying axisymmetric components $(0,k)$ and $(0,-k)$. Similarly, for $\mathrm{WVF_3}$ the dominant components are $(0,\pm k)$ and $(3,\pm k)$.

For visualization purposes, we found the azimuthal vorticity component,

$$\eta = (\nabla\times\mathbf{u})\cdot\mathbf{e}_\theta = \partial_z u - \partial_r w, \tag{2.6}$$

to be an adequate and convenient means to identify and recognize the geometry of complex vortex structures via iso-vorticity surfaces [12,27].

In addition to $\omega_{m,k}$, which reflects the instability, we also consider the global mean angular velocity $\Omega = \langle v/r\rangle_{r,\theta,z}$

(nondimensionalized by Ω_i), which can be different from the azimuthal wave speed $\omega_{m,k}$ of the wavy instability. However, it is the sign of $\omega_{m,k}$ that determines the direction of wave propagation (positive for prograde and negative for retrograde). It is also helpful to visualize isosurfaces azimuthal velocity after subtracting the local azimuthal velocity for circular Couette flow, $v - v_{CCF}$, to show the deviation from stable flow.

III. RESULTS

A. Wavy flow states

Before discussing the wave propagation reversal, we briefly describe the different wavy patterns that can occur for the range of parameters that we consider: wavy flows WVF_2 and WVF_3, which have either twofold or threefold azimuthal periodicity, as illustrated in Fig. 1. As we show later, either state can exist with prograde or retrograde characteristics. The azimuthal symmetry of the states is most obvious in the contours of the azimuthal velocity component v in (r,θ) plane at mid-height [Fig. 1(d)] and also visible in the contours of the radial velocity $u(\theta,z)$ on an unrolled cylindrical surface at mid-gap [Fig. 1(a)]. The isosurfaces of azimuthal vorticity η give an impression of the flow structures of both wavy states. The spatio-temporal character of WVF_2 can be seen, for instance, in WVF2Ri223Ro-145.avi in the Supplemental Materials [28]. For the parameters in Fig. 1 (WVF_2 at $Re_i = 223$ and WVF_3 at $Re_i = 200$, both with $Re_o = -145$) both flow states have prograde wave propagation in that the waves follow the inner cylinder rotation (indicated by the arrows below the images). However, the two wavy states differ in that they have different axial wave numbers k (wavelengths λ) due to different numbers of vortex pairs in the annulus. WVF_2 has five vortex pairs resulting in an axial wave number $k = 3.148$ ($\lambda = 1.996$), while WVF_3 has one additional vortex pair (in total six), which results in an axial wave number $k = 3.769$ ($\lambda = 1.667$).

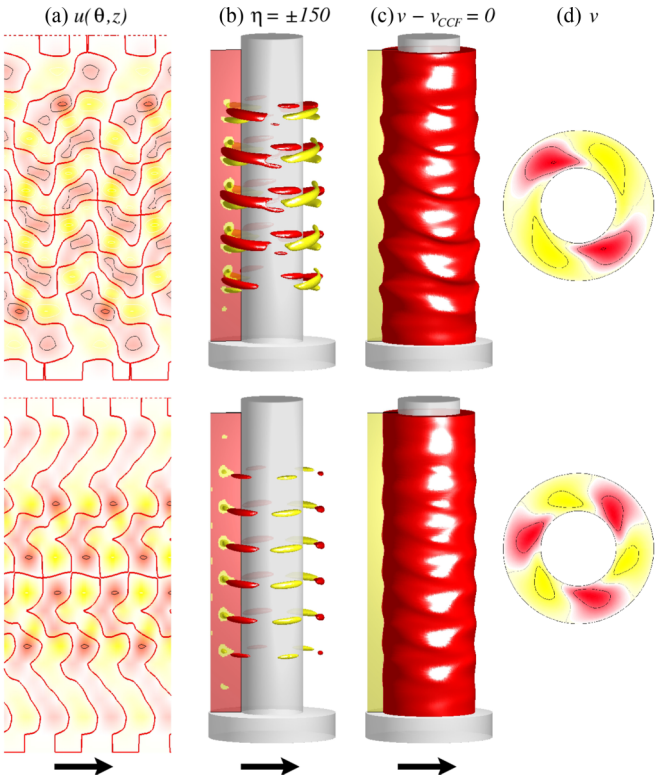

FIG. 1. Prograde flow states WVF_2 and WVF_3. Flow states at $Re_o = -145$ for WVF_2 (top at $Re_i = 223$) and WVF_3 (bottom at $Re_i = 200$). Both wavy flows are prograde in the sense of following the inner cylinder rotation (arrows below the images). Shown are (a) radial velocity $u(\theta,z)$ on an unrolled cylindrical surface in the annulus at mid-gap [red (yellow) color indicates in (out) flow], (b) isosurfaces of azimuthal vorticity η [red (yellow) color indicates positive (negative) vorticity], (c) isosurface of zero azimuthal velocity after subtracting the local azimuthal velocity for circular Couette flow, $v - v_{CCF}$, and (d) the azimuthal velocity component v in (r,θ) plane at mid-height (viewed from the bottom) [red (yellow) color indicates positive (negative) velocity]. (See also corresponding dominant mode amplitudes in WVF2Ri223Ro-145.avi in Supplemental Materials [28].)

B. Flow pattern reversal

Given this context, we can now examine the wave propagation reversal in more detail. For this we focus on the WVF_2 case, setting the outer cylinder rotation at $Re_o = -145$ and varying only Re_i starting with the condition shown in the top panels of Fig. 1. The mechanism for the wave propagation reversal of WVF_3 is similar.

1. Flow dynamics and spatio-temporal behavior

Figure 2 illustrates four snapshots of WVF_2 for fixed outer Reynolds number ($Re_o = -145$) and increasing Re_i from left to right. After its appearance via a supercritical, SO(2) symmetry-breaking, Hopf bifurcation from TVF5 (that is, TVF with five vortex pairs) at $Re_i \approx 197.4$ the WVF_2 flow pattern first follows the rotation of the inner cylinder—it is prograde [Fig. 2(a)]. As Re_i increases, the rotation of the wave pattern stops at $Re_i \approx 224.8$. Above this value for Re_i, the wave pattern rotates in the opposite direction so it is retrograde [Fig. 2(b), 2(c)]. Further increasing Re_i for WVF_2 eventually results in prograde wave propagation for $Re_i = 350$ [Fig. 2(d)] with the change occurring at $Re_i \approx 348.9$. Although the isosurface snapshots indicate that the flow becomes more complex with increasing Re_i, the twofold symmetry is maintained, as is obvious in the cross-section plots of the azimuthal velocity components (bottom in Fig. 2). Moreover the increase of waviness, i.e., the amplitude of the axial variation of the vortices, is visible in the snapshots of the flow. The waviness appears strongest for retrograde case at $Re_i = 330$. For the higher $Re_i = 350$, for which the wave propagation is prograde again, the waviness weakens. The spatio-temporal flow behaviors at different Re_i can be viewed as movies in the Supplemental Materials [28] (movieA1.avi, movieA2.avi, movieA3.avi, movieA4.avi, movieA5.avi, and movieA6.avi). Note that with increasing Re_i, the vortex structures start close to the inner cylinder but move toward the outer cylinder with increasing Re_i.

The WVF_3 case behaves in the same way as WVF_2 for the change to retrograde wave propagation (but for different values of Re_i). Figure 3 illustrates the flow state WVF_3 in the retrograde wave propagation regime at $Re_i = 218$ with Fig. 3(d) clearly highlighting the threefold azimuthal

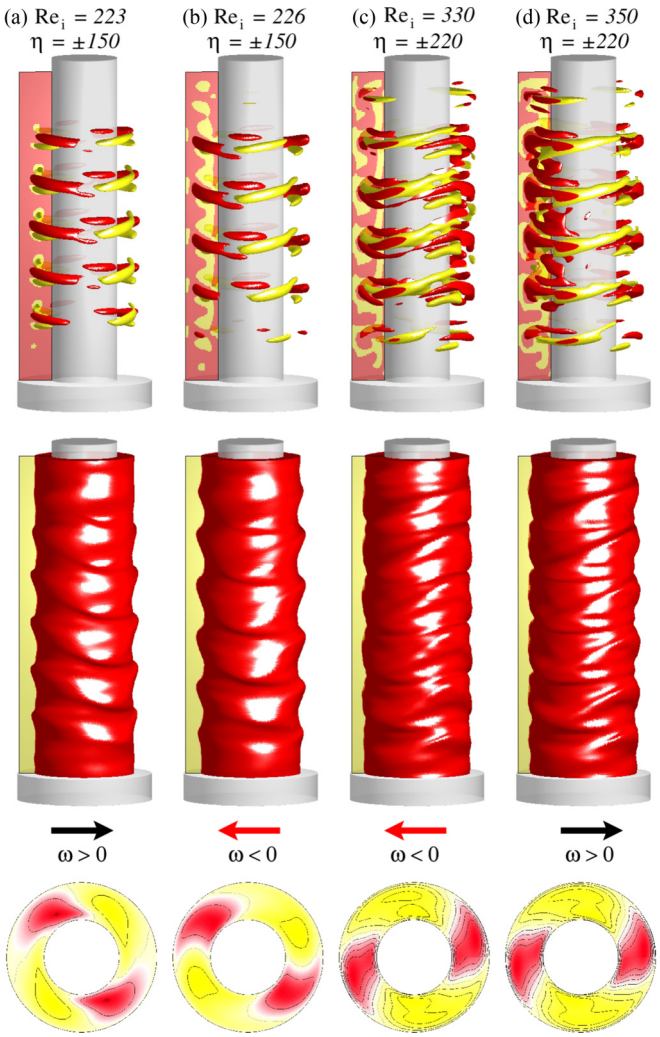

FIG. 2. Flow pattern reversal for WVF_2 with $Re_o = -145$ for prograde ($\omega > 0$) and retrograde situations ($\omega < 0$) at different Re_i as indicated. *Top row:* isosurfaces of azimuthal vorticity η [red (yellow) color indicates positive (negative) vorticity]. *Middle row:* isosurfaces of zero azimuthal velocity after subtracting the local azimuthal velocity for circular Couette flow, $v - v_{CCF}$. *Bottom row:* Contours of azimuthal velocity component v in the (r,θ) plane at mid-height (viewed from the bottom) [red (yellow) color indicates positive (negative) velocity].

symmetry of WVF_3. Since the distance from the flow pattern inversion point is relatively small, the flow pattern looks very similar to the prograde one shown in Fig. 1 (bottom). As is the case for WVF_2, the strength of waviness, i.e., the azimuthal modulation amplitude, is larger in retrograde situation. Unlike the WVF_2 case, the WVF_3 case does not return to prograde wave propagation as Re_o increases, as it becomes unstable at $Re_i \approx 218.6$, after the first change in its propagation direction.

2. *Bifurcation scenario*

The bifurcation scenarios with $Re_o = -145$ and increasing Re_i for both WVF_2 and WVF_3 are presented in Fig. 4. Figure 4(a) shows the dominant radial flow field amplitudes $|u_{m,k}|$ at mid-gap and mid-height. The lowest Re_i in the figure corresponds to the stable base state with only Ekman vortices

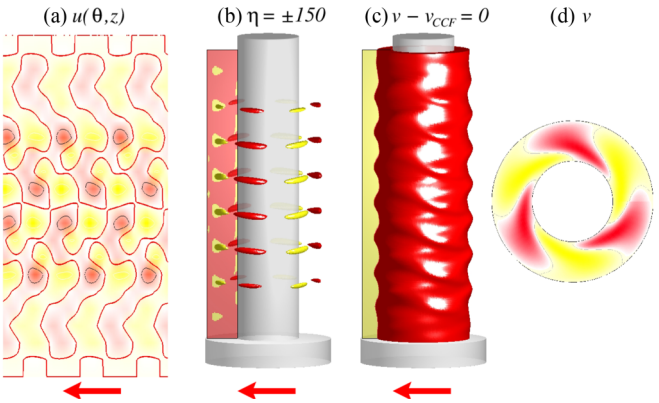

FIG. 3. Retrograde flow state for WVF_3 at $Re_i = 218$ and $Re_o = -145$. The wave propagation is retrograde ($\omega < 0$) in that it is opposite that of the inner cylinder rotation (arrows below the images). Shown are (a) radial velocity $u(\theta,z)$ on an unrolled cylindrical surface in the annulus at mid-gap [red (yellow) color indicates in (out) flow], (b) isosurfaces of vorticity η [red (yellow) color indicates positive (negative) vorticity], (c) isosurface of zero azimuthal velocity after subtracting the local azimuthal velocity for circular Couette flow, $v - v_{CCF}$ and (d) the azimuthal velocity component v in (r,θ) plane at midheight (view from the bottom) [red (yellow) color indicates positive (negative) velocity].

(Ek) at the endwalls [26]. As Re_i increases, first TVF appears at $Re_i \approx 168.3$. Stable TVF can have either five or six vortex cells, denoted as TVF5 ($k = 3.148$) and TVF6 ($k = 3.769$), respectively. With increasing Re_i both TVF conditions lose stability against wavy vortex flow solutions, which appear as a supercritical Hopf bifurcation. Specifically, TVF6 loses stability to WVF_3 at $Re_i \approx 187.6$, and TVF5 loses stability to WVF_2 at $Re_i \approx 197.4$ [marked by x's in Fig. 4(a)]. Note that beyond these points, TVF only exists as unstable solutions (dashed lines) for higher Re_i, based on calculations in the axisymmetric $m = 0$ subspace. As Re_i increases, the $|u_{0,k}|$ mode of the wave solution continues to increase, while the $|u_{2,3.148}|$ begins to grow for WVF_2 and the $|u_{3,3.769}|$ begins to grow for WVF_3. WVF_2 exists over the entire parameter regime that was investigated (up to $Re_i = 400$), while WVF_3 only exists in a relatively narrow range just above transition from TVF6. At $Re_i \approx 218.6$, WVF_3 becomes unstable and moves toward the WVF_2 solution [indicated by the vertical arrows in Fig. 4(a) for both the $|u_{0,3.769}|$ mode and the $|u_{2,3.769}|$ mode]. The only remaining stable solution above $Re_i \approx 218.6$ is WVF_2 which includes the $|u_{0,3.148}|$ and the $|u_{2,3.148}|$ modes. Starting with WVF_2 at large values of Re_i and decreasing Re_i, the flow ends up in TVF5 and never returns to the WVF_3 state. [Arrows along the curves in Fig. 4(a), 4(b) highlight the existence of states with increasing and decreasing Re_i, respectively]. This results in a region of bistability for WVF_2 and WVF_3. The gray shaded regions highlight the range of Re_i for which the retrograde behavior occurs for WVF_2 ($224.8 \lesssim Re_i^{rev} \lesssim 348.9$) and WVF_3 ($210.5 \lesssim Re_i^{rev} \lesssim 218.6$). Clearly, the retrograde behavior does *not* coincide with the transitions from one vortical state to another and therefore does not involve a change in the azimuthal wave number.

The bifurcation scenarios for the modal kinetic energy E_{kin} [Eq. (2.5)] with changing Re_i for both WVF_2 and WVF_3 are

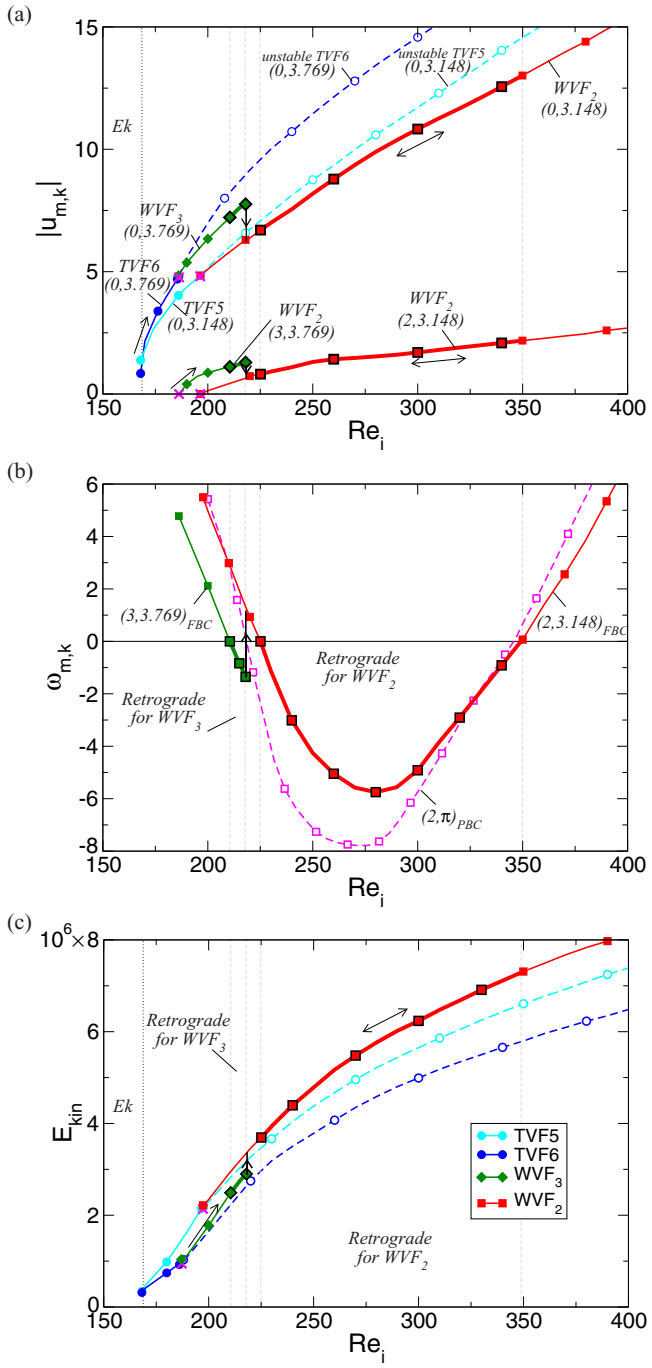

FIG. 4. Bifurcation behavior with $\mathrm{Re_i}$. Variation with $\mathrm{Re_i}$ of (a) moduli $|u_{m,k}|$ of the dominant axial Fourier amplitudes of the azimuthal modes $u_m(z,t)$ [Eq. (2.4)] of the radial flow at mid-gap and the corresponding frequencies, (b) the modal kinetic energy E_{kin} [Eq. (2.5)], and (c) $\omega_{m,k}$ for the flow states, TVF5, TVF6, $\mathrm{WVF_2}$, and $\mathrm{WVF_3}$ (symbols primarily distinguish different structures, but do not represent the resolution of the calculations, which varies depending on the proximity with respect to the wave propagation reversal). Solid (dashed) lines with filled (open) symbols refer to stable (unstable) states. The x's mark the onset of $\mathrm{WVF_2}$ and $\mathrm{WVF_3}$ from TVF5 and TVF6, respectively. Thick lines indicate retrograde wave propagation ($\omega < 0$) for $\mathrm{WVF_3}$ and $\mathrm{WVF_2}$, respectively. Outer Reynolds number is fixed: $\mathrm{Re_o} = -145$. For comparison, the dashed line with open squares in (c) shows the frequency for simulations with periodic boundary conditions for $k = \pi$, which corresponds to $\Gamma = 2$.

shown in Fig. 4(b). Here it is evident that the TVF5 flow is more energetic than the TVF6 flow, leading to $\mathrm{WVF_2}$ being more energetic than $\mathrm{WVF_3}$ until $\mathrm{WVF_3}$ loses stability to $\mathrm{WVF_2}$ flow at $\mathrm{Re_i} \approx 218.6$ (vertical arrow).

To confirm that the wave propagation reversal is intrinsic to the system and not induced by the fixed boundary conditions (FBC, corresponding to non-rotating end walls, which necessarily force Ekman pumping), we also carried out simulations with periodic boundary conditions (PBC) instead of fixed (non-rotating) end walls, which is equivalent to infinitely long cylinders. To do so, we set the axial wave number to $k = \pi$ which is fairly close to the value $k = 3.148$ that is naturally selected by the system for $\mathrm{WVF_2}$ at $\Gamma = 10$. Note, that we do not force an azimuthal wave number. This dominant $m = 2$ azimuthal periodicity is natural selected by the system. Qualitatively, the dynamics is the same for PBC and FBC, as demonstrated for $\mathrm{Re_o} = -145$ in Fig. 4(c) illustrating the corresponding frequencies $\omega_{m,k}$ of the dominant axial Fourier amplitudes $u_m(z,t)$. The flow is retrograde (negative frequency) for a similar range of $\mathrm{Re_i}$ for both PBC (dashed curve with open squares) and FBC (solid curve with filled squares), but prograde (positive frequency) both below and above this range for $m = 2$ (gray shaded region). In both cases, upon increasing $\mathrm{Re_i}$ from a low value, the frequency changes sign indicating that the wave propagation is now in opposite direction (retrograde), and at higher $\mathrm{Re_i}$ a second reversal in the pattern propagation direction occurs (back to prograde). However, the reversal points are shifted to slightly lower values of $\mathrm{Re_i}$ for PBC: $\mathrm{Re_i}^{\mathrm{rev},1}(\mathrm{PBC}) \approx 218.2$ and $\mathrm{Re_i}^{\mathrm{rev},2}(\mathrm{PBC}) \approx 346.2$. This is compared to the values for fixed end walls: $\mathrm{Re_i}^{\mathrm{rev},1}(\mathrm{FBC}) \approx 224.8$ and $\mathrm{Re_i}^{\mathrm{rev},2}(\mathrm{FBC}) \approx 348.9$. The slightly different values $\mathrm{Re_i}^{\mathrm{rev},1}$ for PBC compared to FBC may result from the slightly different wave numbers but are well within the accuracy of previous studies comparing experiments and numerics [26]. It is worth mentioning that we also performed simulations with other aspect ratios, $\Gamma = 8, 12, 14$, and observed the same qualitative behavior of flow reversal.

Similar to flow state $\mathrm{WVF_2}$, $\mathrm{WVF_3}$ also changes its wave propagation direction [zero-crossing in the corresponding frequency $\omega_{3,3.769}$ in Fig. 4(c), gray shaded region]. However, above $\mathrm{Re_i} \approx 218.6$ the wavy flow $\mathrm{WVF_3}$ becomes unstable and evolves gradually to the other solution branch, the stable wavy flow state $\mathrm{WVF_2}$. As the latter is still prograde for this $\mathrm{Re_i}$, this change is also accompanied with a wave propagation reversal. But here it results from switching between different solution branches (cf. [18]) and is likely unrelated to the reversal via continuous variation of a single parameters, $\mathrm{Re_i}$ or $\mathrm{Re_o}$. We assume that searching across the parameter space one might also find similar reversal dynamics for wavy vortices with even higher azimuthal wave numbers.

3. *Wavy instability and angular velocity*

To this point, we have fixed the outer Reynolds number at $\mathrm{Re_o} = -145$. Figure 5 shows the dependence of the frequency ω describing the wavy instability and the global mean angular velocity Ω on $\mathrm{Re_i}$ for three different values of $\mathrm{Re_o}$. All curves show qualitatively similar behavior: with increasing $\mathrm{Re_i}$, ω first decreases, reaching a minimal value ω_{min}, and then it

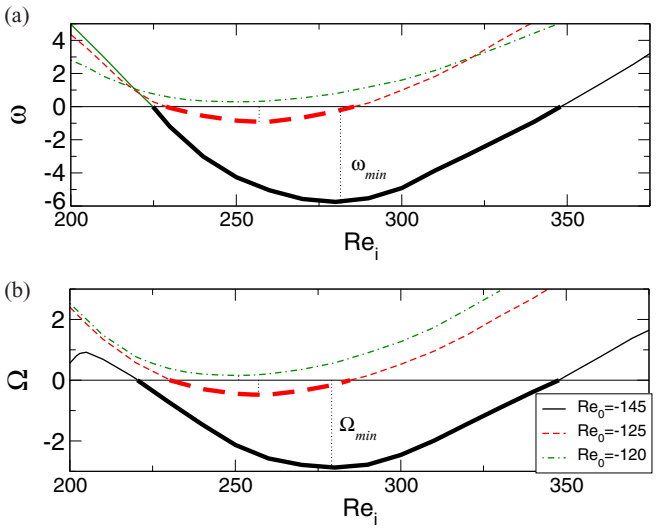

FIG. 5. Variation with $\mathrm{Re_i}$ of wavy instability ω and angular velocity Ω for $\mathrm{WVF_2}$. Variation with $\mathrm{Re_i}$ of (a) wavy instability frequency ω, characterizing the rotation of the wave pattern, for $\mathrm{WVF_2}$ at $\mathrm{Re_o}$ as indicated. Also shown is the corresponding (b) global mean angular velocity Ω representing the overall azimuthal flow. Vertical dotted lines indicate the minima $\omega_{\min}$ and $\Omega_{\min}$, respectively.

increases again. Depending on $\mathrm{Re_o}$ the curve can extend below $\omega = 0$, which indicates retrograde flow. It is interesting that the minimum value $\omega_{\min}$ occurs at values of the Reynolds number ratio $-\mathrm{Re_i}/\mathrm{Re_o}$ near two for the parameter regime investigated here, as will be discussed shortly. The curves for the angular velocity Ω in Fig. 5(b) show qualitatively the same behavior. In fact, they differ only slightly in the values for zero-crossing Retrograde propagation based on ω appears for $\mathrm{Re_o} = -145$ at $\mathrm{Re_i^{rev,1}} = 224.8$, $\mathrm{Re_i^{rev,2}} = 348.9$ and for $\mathrm{Re_o} = -125$ at $\mathrm{Re_i^{rev,1}} = 228.8$, $\mathrm{Re_i^{rev,2}} = 285.6$. Note that for $\mathrm{Re_o} = -120$ the flow is always prograde with no zero-crossing. The corresponding angular velocities Ω for retrograde propagation are slightly different, appearing for $\mathrm{Re_o} = -145$ at $\mathrm{Re_i^{rev}}(\Omega = 0) = 220.4$, $\mathrm{Re_i^{rev}}(\Omega = 0) = 347.8$ and for $\mathrm{Re_o} = -125$ at $\mathrm{Re_i^{rev}}(\Omega = 0) = 230.1$, $\mathrm{Re_i^{rev}}(\Omega = 0) = 284.7$.

This highlights that the propagation of the wavy instability is closely linked to the overall azimuthal flow.

4. Parameter space

Figure 6 presents the parameter space spanned by the inner and outer Reynolds numbers $\mathrm{Re_i}$ and $\mathrm{Re_o}$ for which the wavy flow shows retrograde wave propagation behavior for $\mathrm{WVF_2}$. For $\mathrm{Re_o} \gtrsim -123$, the wave propagation is prograde ($\omega > 0$), regardless of $\mathrm{Re_i}$. This corresponds to situations like that shown in Fig. 5 for $\mathrm{Re_o} = -120$. For $\mathrm{Re_o} \lesssim -124$, the wave propagation is retrograde ($\omega < 0$) for a broadening band of $\mathrm{Re_i}$ as $\mathrm{Re_o}$ decreases, corresponding to the situation shown in Fig. 5 for $\mathrm{Re_o} = -125$ and $\mathrm{Re_o} = -145$. The value of $\mathrm{Re_i}$ for which $\omega_{\min}$ occurs increases monotonically with decreasing $\mathrm{Re_o}$. Note the narrow band of values for which $\omega < 0$ for $\mathrm{WVF_3}$ below the large shaded area for $\mathrm{WVF_2}$. The striped region at the right end of the line symbolizes that $\mathrm{WVF_3}$ becomes unstable such that we could not follow this solution further.

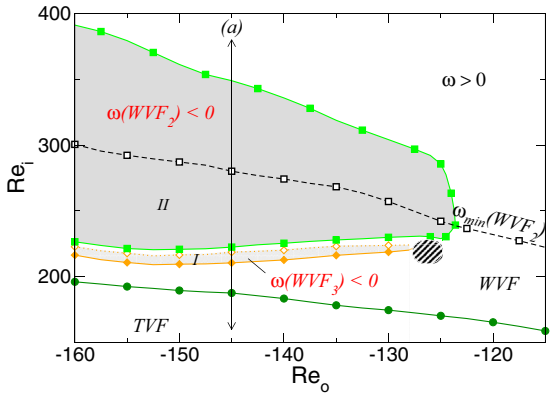

FIG. 6. Parameter space diagram ($\mathrm{Re_i}$,$\mathrm{Re_o}$). Parameter space diagram illustrating stability and rotation direction of wavy flows pattern. Gray colored regions indicate wavy flow patterns of $\mathrm{WVF_3}$ (I) and $\mathrm{WVF_2}$ (II) with retrograde ($\omega < 0$) behavior. The curve with squares (■) highlights where $\omega = 0$ in the laboratory frame. The analogous curve with diamonds (♦) illustrates the where $\omega = 0$ for $\mathrm{WVF_3}$. Below this curve $\mathrm{WVF_3}$ is prograde and above it retrograde. The striped region at the right end of the curve indicates that $\mathrm{WVF_3}$ becomes unstable, and we could not follow this solution further. The dotted curve indicates the loss of stability for $\mathrm{WVF_3}$ with increasing $\mathrm{Re_i}$. The lowest curve with circles (●) indicates the onset of wavy flows, independent of their azimuthal wave number; below this curve only stable TVF exists. The dashed line with open squares (□) depicts the minima $\omega_{\min}$ in case of $\mathrm{WVF_2}$. The vertical arrow (a) indicates the parameter range of the bifurcation diagrams of Fig. 4.

It is worth noting that the region of wave propagation reversal surrounding the line $\mathrm{Re_i} = -2\mathrm{Re_o}$, which corresponds to equal and opposite cylinder surface speeds, $\Omega_i R_i = \Omega_o R_o$, for a radius ratio $R_i/R_o = 0.5$. Well above this line, one would expect the inner cylinder to dominate the overall flow such that $\Omega > 0$. Just as the wave propagation tends to be in the same direction as the overall flow for standard WVF with a rotating inner cylinder and fixed outer cylinder [8–16,19], wave propagation is prograde (with the inner cylinder) when $\Omega > 0$ for the counter-rotating cylinders here. Around the line $\mathrm{Re_i} = 2\mathrm{Re_o}$ and below it, it is reasonable to expect the outer cylinder to dominate the flow (hence, $\Omega \leqslant 0$, as shown in Fig. 5(a) and 5(b)). This leads to retrograde wave propagation, since, again, the wave propagation tends to be in the same direction as the overall flow.

The question is why does the wave propagation (and Ω) return to prograde for well below the line $\mathrm{Re_i} = -2\mathrm{Re_o}$? The answer may be in the nature of the instability, which is associated with the inviscidly unstable region near the inner cylinder. Since the unstable region for counter-rotating cylinders is nearer the inner cylinder [29], it is reasonable that its propagation coincides with the flow near the inner cylinder and is $-2\mathrm{Re_o}$ in which the retrograde propagation of the instability can occur. This point is supported by the location of the vortex structures for different $\mathrm{Re_i}$. While they are close to the inner cylinder at lower $\mathrm{Re_i}$ (Fig. 1, bottom row) they move outward with increasing $\mathrm{Re_i}$ toward the outer region (Fig. 2, bottom row). Furthermore, above the transition from TVF5 to $\mathrm{WVF_2}$ at $\mathrm{Re_i} \approx 197.4$, the angular velocity Ω, grows more positive with increasing $\mathrm{Re_i}$, reaching a maximum at

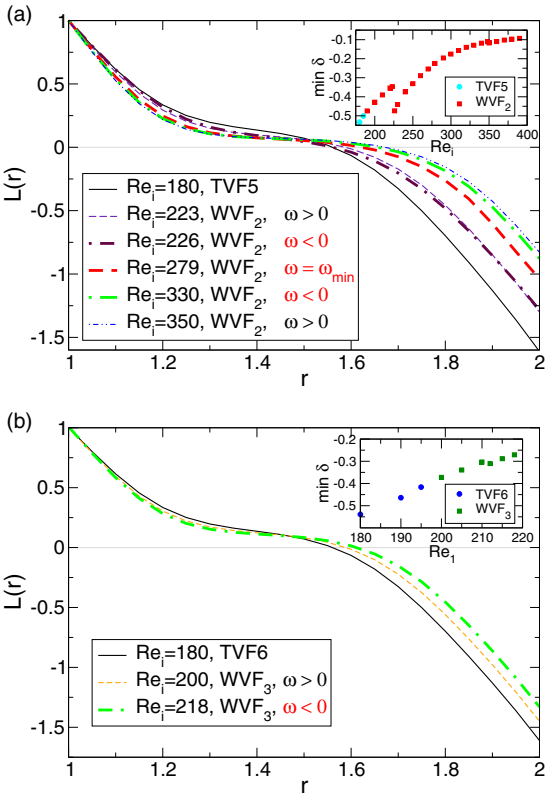

FIG. 7. Variation in angular momentum for WVF_2 and WVF_3. Angular momentum $L(r) = r\langle v(r)\rangle_{\theta,z}/\mathrm{Re_i}$ versus the radius r for wavy solutions with increasing $\mathrm{Re_i}$ as indicated for (a) TVF5 and WVF_2 and (b) TVF6 and WVF_3. Outer Reynolds number is fixed at $\mathrm{Re_o} = -145$. The insets show the variation with $\mathrm{Re_i}$ of minimum of slopes $\delta = \partial L/\partial r$.

$\mathrm{Re_i} \approx 205$ and decreasing again [see inset in top panel in Fig. 5(b)] to eventually become negative at the $\mathrm{Re_i}$ where the retrograde propagation occurs.

5. *Angular momentum transport*

To attempt to characterize the wave propagation reversal phenomenon, we examine the behavior of the angular momentum and torque for a variety of flow conditions that are both prograde ($\omega > 0$) and retrograde ($\omega < 0$). Figure 7 shows the mean (axially and azimuthally averaged) angular momentum $L(r) = r\langle v(r)\rangle_{\theta,z}/\mathrm{Re_i}$, as a function of the radius r for different $\mathrm{Re_i}$. Figure 7(a) shows profiles for TVF5 and WVF_2; Fig. 7(b) shows profiles for TVF6 and WVF_3. All curves have a similar shape. In general, the profiles indicate typical behavior in that positive angular momentum decreases outward from the inner cylinder and negative angular momentum decreases inward from the outer cylinder with a region of nearly zero angular momentum in between. With increasing $\mathrm{Re_i}$ the profiles flatten a bit in the middle of the annular gap to form a horizontal plateau, which tends to be slightly closer the inner cylinder than the outer cylinder. In general the angular momentum curves follow a monotonically varying trend. The curves spread near the outer cylinder, but this is simply a consequence of non-dimensionalizing with $\mathrm{Re_i}$. Further, we can compare the curves for prograde and retrograde propagation of the waves. For TVF5 and WVF_2 [Fig. 7(a)], the angular momentum for $\mathrm{Re_i} = 223$, which has prograde propagation of the vortex waves, nearly overlays the curve for $\mathrm{Re_i} = 226$, which has retrograde propagation, indicating no substantial differences in the angular momentum for prograde and retrograde wave propagation. Strictly speaking, the angular momentum curves for $\mathrm{Re_i} = 223$ and $\mathrm{Re_i} = 226$ do not follow the monotonically varying trend evident more generally. The insets in Fig. 7 show the variation with $\mathrm{Re_i}$ for minimum of slopes $\delta = \partial L/\partial r$ for TVF5, TVF6, WVF_2, and WVF_3, respectively. There is a general decrease of the minimum slopes with $\mathrm{Re_i}$, with of non-monotonic behavior at the reversal points. The latter is most evident for the change in WFV_2 from prograde to retrograde,

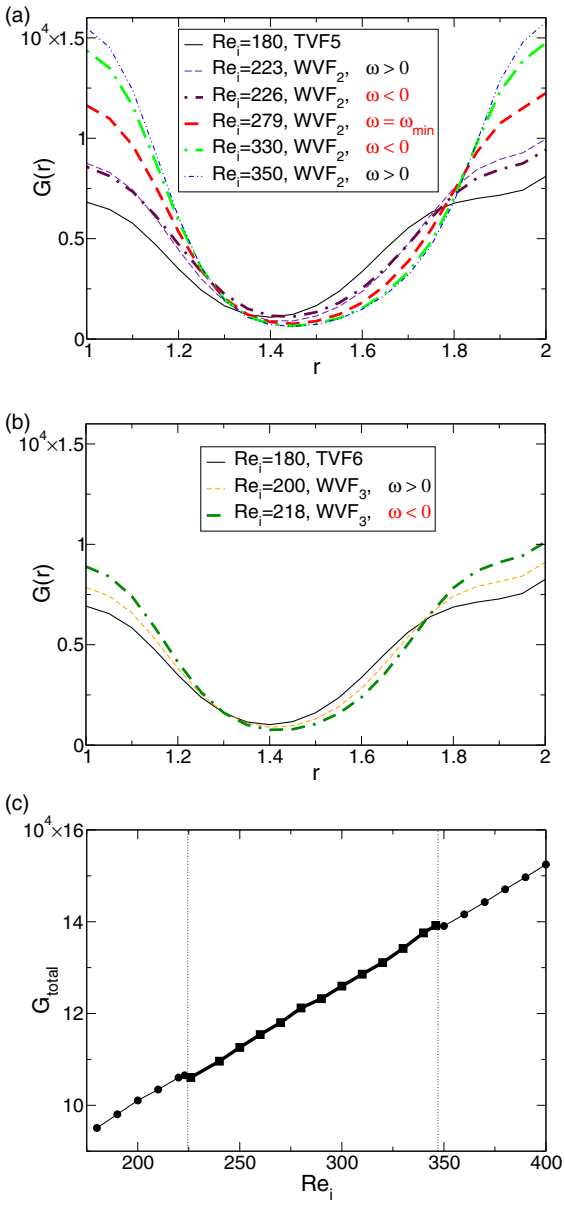

FIG. 8. Variation of dimensionless torque for WVF_2 and WVF_3. Variation of the dimensionless torque $G = \nu J^{\omega}$ (see text for details) versus the radius r for wavy solutions with increasing $\mathrm{Re_i}$ as indicated. (a) TVF5 and WVF_2 and (b) TVF6 and WVF_3. Outer Reynolds number is fixed at $\mathrm{Re_o} = -145$. (c) Dependence of the total torque G_{total} on $\mathrm{Re_i}$ for evolution of TVF5 and WVF_2.

but a slight change in the minimum value of δ is also apparent for its reversal back to prograde and the reversal in WVF_3.

The curves for angular momentum close to the wave propagation reversal from retrograde wave propagation $Re_i = 330$ back to prograde wave propagation at $Re_i = 350$ are also similar. The same similarity in the angular momentum at the wave propagation reversal from prograde to retrograde wave propagation is also evident for TVF6 and WVF_3 [Fig. 7(b)] for $Re_i = 200$ (prograde) and $Re_i = 218$ (retrograde). Note that the curves for TVF5 and TVF6 are almost identical. Thus, it appears that there is no clear correlation between the change from prograde to retrograde wave propagation, or vice versa, and the average angular momentum of the flow.

Figure 8 shows the corresponding variation of the dimensionless torque $G = \nu J^{\omega}$ within the annulus. In calculating the torque we used the fact that for a flow between infinite cylinders the transverse current of the azimuthal motion, $J^{\omega} = r^3[\langle u\omega\rangle_{A,t} - \nu\langle\partial_r\omega\rangle_{A,t}]$ (with $\langle\cdots\rangle_A \equiv \int \frac{rd\theta dz}{2\pi rl}$), is a conserved quantity [30]. With increasing Re_i the "parabola-like" curvature of the torque profiles in the mid-gap region becomes more pronounced. As with the angular momentum, the profiles of $G(r)$ show a generally monotonically varying trend as Re_i increases with very little difference between the curves just above and just below the prograde-to-retrograde and retrograde-to-prograde changes. Again one might argue that the curves for $Re_i = 223$ and $Re_i = 226$ do not strictly follow this monotonically varying trend, though the differences between the two curves is small. The result of this is also evident in the total torque G_{total}, which increases linearly with Re_i [Fig. 8(c)] except at the values for Re_i corresponding the reversal of the pattern. Around these values G_{total} has a small plateau. Nevertheless, the changes are so slight that it is hard to infer much about the physics from this.

IV. SUMMARY

We have identified conditions of supercritical wavy vortex flow in a relatively wide gap between counter-rotating cylinders in which the wave propagation reverses upon the variation of a single system parameter while maintaining the azimuthal wave number. This wave propagation reversal occurs for both wavy flow states, WVF_2 and WVF_3, which have twofold and threefold azimuthal symmetry, respectively, upon changing either the inner or outer cylinder rotation speed. The prograde wave propagation slows down with continuously increasing Re_i, becomes zero, and restarts motion in the opposite direction to become retrograde. Upon increasing the angular velocity of the inner cylinder further, the azimuthal speed of the wavy instability of the retrograde waves becomes more negative, but eventually reverses its trend, and finally vanishes a second time returning to prograde wave propagation again. This is different from previous studies in which the propagation of the waviness changes direction [18] in that wave propagation reversal here does not coincide with changes in the dominant azimuthal wave number in the wavy state.

The wave propagation reversal instead coincides with the reversal of the global mean angular velocity. This suggests that the propagation of the waviness is directly connected to the overall azimuthal mean flow. As the unstable region for counter-rotating cylinders is nearer the inner cylinder, it is reasonable that its propagation initially coincides with the flow the inner cylinder after transition from TVF to WVF and is thereby prograde. However, in the region around the line $Re_i = -2Re_o$ in which $\Omega_i R_i = \Omega_o R_o$ for a radius ratio $R_i/R_o = 0.5$, retrograde propagation of the instability can occur. Here the vortices fill the annulus, and the wave propagation is driven by the outer cylinder rotation. As Re_i increases well above this line, the inner cylinder dominates so the waves revert to prograde propagation with the inner cylinder.

The flow pattern propagation reversal is *intrinsic* to the system in that simulations with periodic boundary conditions in place of a finite length annulus also result in the wave propagation reversal. Hence, the wave propagation reversal is *not* induced by end-wall effects, such as Ekman pumping. Moreover, simulations for other aspect ratios ($\Gamma = 8, 12, 14$) further illustrate that the wave propagation reversal is inherent general to the system, though the values for the appearance of wave propagation reversal depend on the aspect ratio. It is possible that by searching over a wider parameter range one might find similar reversal dynamics for wavy vortices with higher azimuthal wave numbers. This might provide further insight into the mechanism for wave propagation reversal.

[1] H. Swinney and J. Gollub, *Hydrodynamic Instabilities and the Transition to Turbulence* (Springer, Berlin, 1981).

[2] T. Mullin, *The Nature of Chaos* (Oxford University Press, New York, 1994).

[3] C. Egbers and G. Pfister, *Physics of Rotating Fluids* (Springer, Berlin, 2000).

[4] A. Gill, *Atmosphere-Ocean Dynamics* (Academic Press, San Diego, 1982).

[5] A. Davey, R. C. Di Prima, and J. T. Stuart, J. Fluid Mech. **31**, 17 (1968).

[6] G. Iooss, J. Fluid Mech. **173**, 273 (1986).

[7] S. Altmeyer, Y. Do, F. Marques, and J. M. Lopez, Phys. Rev. E **86**, 046316 (2012).

[8] D. Coles, J. Fluid Mech. **21**, 385 (1965).

[9] S. T. Wereley and R. M. Lueptow, J. Fluid Mech. **364**, 59 (1998).

[10] C. A. Jones, J. Fluid Mech. **102**, 249 (1981).

[11] G. P. King, Y. Li, W. Lee, H. L. Swinney, and P. S. Marcus, J. Fluid Mech. **141**, 365 (1984).

[12] C. Hoffmann, S. Altmeyer, A. Pinter, and M. Lücke, New J. Phys. **11**, 053002 (2009).

[13] G. Ahlers, D. S. Cannell, and M. A. Dominguez Lerma, Phys. Rev. A **27**, 1225(R) (1983).

[14] P. S. Marcus, J. Fluid Mech. **146**, 65 (1984).

[15] W. Schröder and H. B. Keller, J. Comp. Phys. **91**, 197 (1990).

[16] A. Akonur and R. M. Lueptow, Phys. Fluids **15**, 947 (2003).

[17] S. Altmeyer, Y. Do, and Y.-C. Lai, Phys. Rev. E **92**, 053018 (2015).

[18] D. Martinand, E. Serre, and R. Lueptow, Phys. Fluids **26**, 094102 (2014).
[19] C. C. Andereck, S. S. Liu, and H. L. Swinney, J. Fluid Mech. **164**, 155 (1986).
[20] S. Altmeyer, Y. Do, and Y.-C. Lai, Scientific Reports **5**, 18589 (2015).
[21] D. Martinand, E. Serre, and R. M. Lueptow, Phys. Fluids **21**, 104102 (2009).
[22] P. Chossat and G. Iooss, *The Couette-Taylor Problem* (Springer, Berlin, 1994).
[23] G. I. Taylor, Phil. Trans. Roy. Soc. Lond. A **223**, 289 (1923).
[24] S. Hughes and A. Randriamampianina, Intnl J. Num. Meth. Fluids **28**, 501 (1998).
[25] I. Mercader, O. Batiste, and A. Alonso, Comput. Fluids **39**, 215 (2010).
[26] S. Altmeyer, C. Hoffmann, M. Heise, J. Abshagen, A. Pinter, M. Lücke, and G. Pfister, Phys. Rev. E **81**, 066313 (2010).
[27] S. Altmeyer and C. Hoffmann, New J. Phys. **12**, 113035 (2010).
[28] See Supplemental Material at http://link.aps.org/supplemental/10.1103/PhysRevE.95.053103 for movies illustrating the spatio-temporal characteristics of WVF_2 solution.
[29] O. Czarny, E. Serre, P. Bontoux, and R. M. Lueptow, Theoret. Comput. Fluid Dynamics **18**, 151 (2004).
[30] B. Eckhardt, S. Grossmann, and D. Lohse, J. Fluid Mech. **581**, 221 (2007).